

High-pressure synthesis of Ba₂RhO₄, a rhodate analogue of the layered perovskite Sr-ruthenate

I. Kurata,^{1,2} José A. Flores-Livas,³ H. Sugimoto,² H. Takahashi,^{1,4} H. Sagayama,⁵ Y. Yamasaki,⁶ T. Nomoto,² R. Arita,^{2,7} and S. Ishiwata^{1,4}

¹*Division of Materials Physics, Graduate School of Engineering Science, Osaka University, Osaka 560-8531, Japan*

²*Department of Applied Physics, University of Tokyo, Tokyo 113-8656, Japan*

³*Dipartimento di Fisica, Università di Roma La Sapienza, Piazzale Aldo Moro 5, I-00185 Roma, Italy*

⁴*Center for Spintronics Research Network (CSRN), Graduate School of Engineering Science, Osaka University, Osaka 560-8531, Japan*

⁵*Institute of Materials Structure Science, High Energy Accelerator Research Organization, Tsukuba, Ibaraki 305-0801, Japan*

⁶*Research and Services Division of Materials Data and Integrated System (MaDIS), National Institute for Materials Science (NIMS), Ibaraki, Tsukuba 305-0047, Japan*

⁷*RIKEN Center for Emergent Matter Science, 2-1 Hirosawa, Wako, 351-0198, Japan*

(Dated: March 17, 2024)

A new layered perovskite-type oxide Ba₂RhO₄ was synthesized by a high-pressure technique with the support of convex-hull calculations. The crystal and electronic structure were studied by both experimental and computational tools. Structural refinements for powder x-ray diffraction data showed that Ba₂RhO₄ crystallizes in a K₂NiF₄-type structure, isostructural to Sr₂RuO₄ and Ba₂IrO₄. Magnetic, resistivity, and specific heat measurements for polycrystalline samples of Ba₂RhO₄ indicate that the system can be characterized as a correlated metal. Despite the close similarity to its Sr₂RuO₄ counterpart in the electronic specific heat coefficient and the Wilson ratio, Ba₂RhO₄ shows no signature of superconductivity down to 0.16 K. Whereas the Fermi surface topology has reminiscent pieces of Sr₂RuO₄, an electron-like e_g-(d_{x₂-y₂) band descends below the Fermi level, making of this compound unique also as a metallic counterpart of the spin-orbit-coupled Mott insulator Ba₂IrO₄.}

I. INTRODUCTION

Layered perovskite-type oxides A₂MO₄ (A: Rare-earth metal or alkaline earth metal; M: transition metal) have been extensively studied as two-dimensional correlated electron systems showing exotic electronic properties. This is typified by La_{2-x}Sr_xCuO₄ and Sr₂RuO₄ showing unconventional superconductivity¹⁻⁵ and Sr₂CoO₄ showing ferromagnetic and metallic behavior⁶. Because of the close analogy to La₂CuO₄, Sr₂IrO₄ has recently attracted great attentions.⁷⁻⁹ The ground state of Sr₂IrO₄ has been described as a spin-orbit coupled Mott insulating state with antiferromagnetic ordering.¹⁰ In A₂MO₄, symmetry and local distortion of the M-O square lattice, which depend on the size of A-site ion, seem to play an important role for their electronic ground states. For instance, Sr₂RuO₄ has tetragonal symmetry with straight Ru-O-Ru bonds, whereas Ca₂RuO₄ known as an antiferromagnetic Mott insulator has large distortion of the Ru-O-Ru bonds¹¹. Recently, Ba₂IrO₄ has been synthesized by a high pressure technique and found to be tetragonal with straight Ir-O-Ir bonds, which are in contrast to those of Sr₂IrO₄ with orthorhombic distortion¹². Reflecting the absence of the lattice distortion, the magnetic ground state of Ba₂IrO₄ is free from the spontaneous magnetic moment caused by the Dzyaloshinskii-Moriya interaction, unlike the case of Sr₂IrO₄.

As mentioned above, Sr₂RuO₄ and Ba₂IrO₄ share the same tetragonal layered perovskite-type structure but show contrasting ground states. Therefore, it is tempting to explore novel electronic states in their relatives.

Following this viewpoint, we take focus on the rhodium analogue, that is Sr₂RhO₄ with moderate electron correlation and spin-orbit coupling (SOC)¹³⁻¹⁶. So far, solid solutions between Sr₂RhO₄ and the known compounds such as Sr₂Rh_{1-x}Ir_xO₄¹⁷ and Sr_{2-x}La_xRhO₄¹⁸ have been studied. However, these oxides have a lattice distortion unlike Sr₂RuO₄ and Ba₂IrO₄ with straight M-O-M bonds, which can be critical for the emergence of novel electronic states.

In this work, we succeeded in the high-pressure synthesis of a new layered perovskite rhodate Ba₂RhO₄ and characterized its structural, magnetic, and electronic properties. From Rietveld refinements of the synchrotron x-ray diffraction data, Ba₂RhO₄ was found to crystallize in the tetragonal space group (*I4/mmm*), being isostructural with Sr₂RuO₄. In addition to this first member of Ruddlesden-Popper phases Ba_{n+1}Rh_nO_{3n+1} with *n* = 1, other possible formations of the other phases with *n* = 2, 3, and ∞ (perovskite phase) under high pressures are also predicted in terms of their formation enthalpy. Although the signature of superconductivity has not been found at low temperatures down to 0.16 K, the close similarity to Sr₂RuO₄ counterpart will be discussed.

II. METHOD

A. Experimental details

Polycrystalline samples of Ba₂RhO₄ were prepared by the solid-state reaction with a high-pressure technique

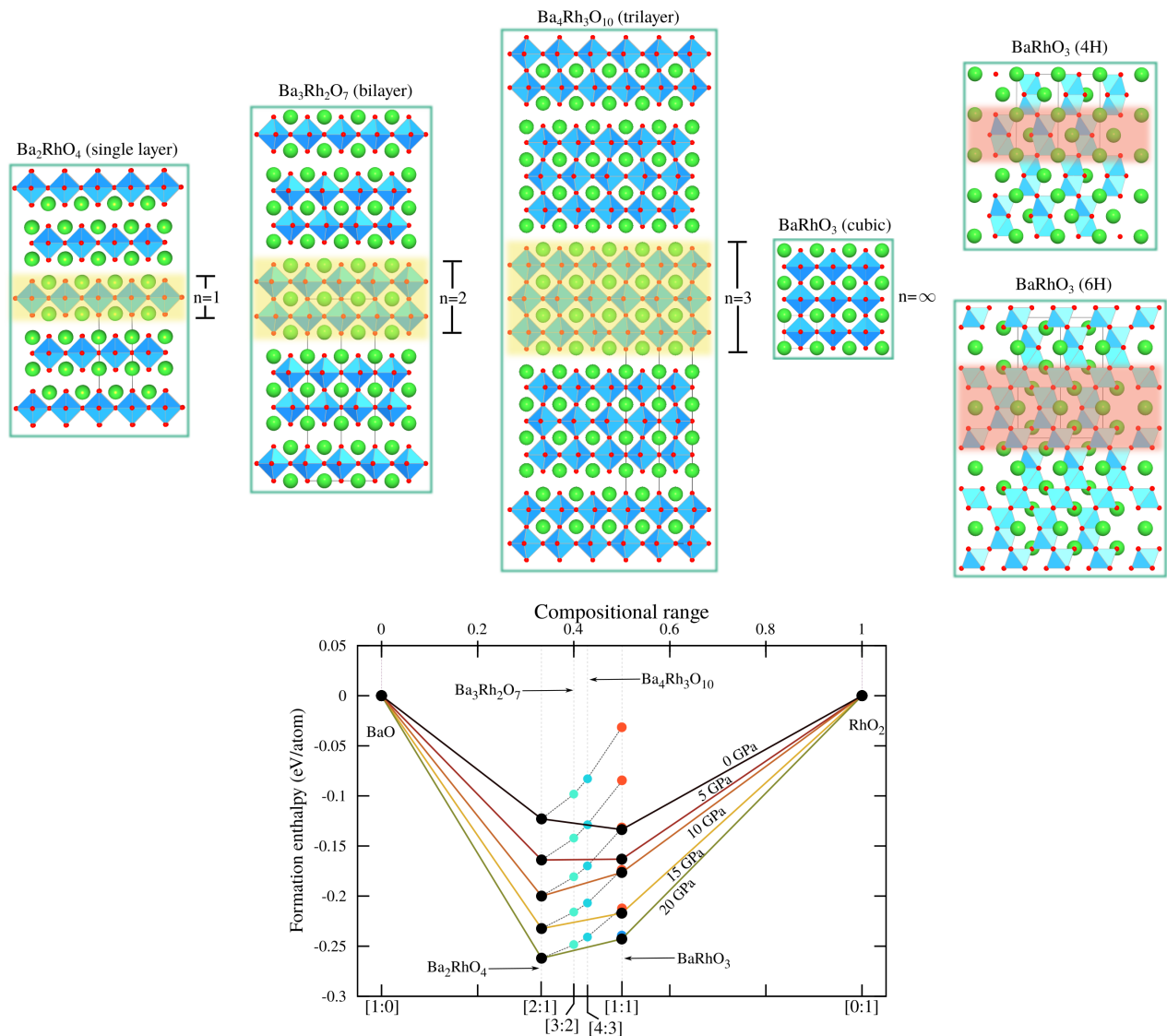


Figure 1. Bottom panel: Convex hull of enthalpy formation calculated for stoichiometries between BaO to RhO₂ as a function of pressure. Solid-black points represent stable compositions in the convex for selected pressures. For readability, the abscissa in the top show composition range and in the bottom composition ratio. Each of the points relates to a crystalline structure (show in the top) for different Ba-rhodates following the Ruddlesden-Popper sequence ($\text{Ba}_{n+1}\text{Rh}_n\text{O}_{3n+1}$).

using a cubic-anvil-type high-pressure apparatus (ME-TEORITE). The stoichiometric mixture of BaO₂ (99.9%, Furuuchi Chemical Co., Ltd.) and Rh metal powder (99.96%, Furuya Metal Co., Ltd.) was encapsulated in a platinum tube in a glove box with a high-purity argon atmosphere. The sample was heated at 1350-1400 °C for 30 min. at 8 GPa, followed by quenching to room temperature before the pressure was released. The polycrystalline sample of Ba₂RhO₄ was obtained as a dense and black pellet. As the sample is sensitive to air and moisture, it was kept in a glove box. The purity of the sample was checked by powder x-ray diffraction with Cu K α radiation (BRUKER new D8). The data for structure refinements were collected as well, by synchrotron

powder x-ray diffraction with a wavelength of 0.68975 Å at BL-8B, Photon Factory, KEK, Japan. The diffraction data were analyzed using the Rietveld refinement using RIETAN-FP¹⁹. The resistivity and specific heat were measured by the standard dc four-probe method. Magnetic susceptibility data were collected by a superconducting quantum interference device magnetometer.

B. Computational details

For the convex hull, all structural relaxations at different pressures were evaluated within DFT at the level of the Perdew-Burke-Erzenhof (PBE)²⁰ approximation

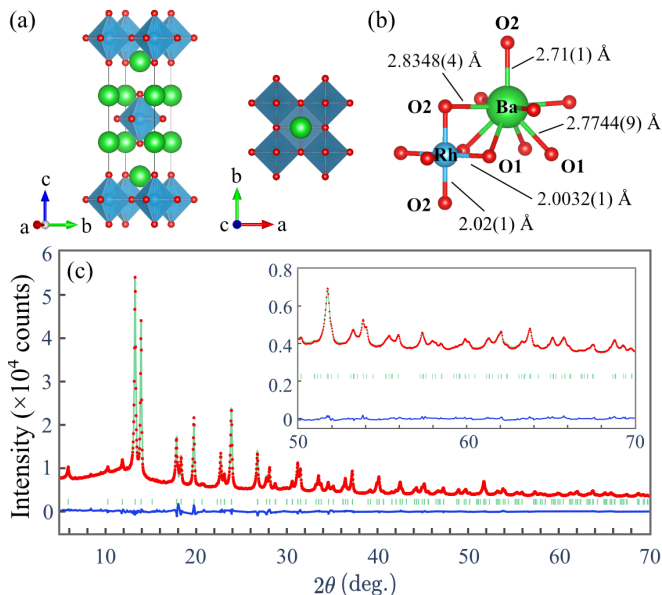


Figure 2. (a) Crystal structure of Ba_2RhO_4 and (b) a schematic representation of the local structure with bond lengths around the Rh and Ba atoms. (c) Observed (red crosses), calculated (green line), and differential (blue line) synchrotron x-ray diffraction patterns. The green tick marks indicate the calculated peak positions.

to the exchange-correlation functional. A plane wave basis-set with a cutoff energy of 900 eV was used to expand the wave-functions together with the projector augmented wave (PAW) method as implemented in the Vienna ab initio Simulation Package VASP²¹. Structures in the convex hull construction were converged to less than two $\text{meV}\text{\AA}^{-1}$. All electronic band structures and magnetic properties were calculated using the full-potential linearized augmented plane-wave (FP-LAPW) method as implemented within the ELK code^{22,23}. We took into account spin-orbit-coupling (SOC) and performed a fully non-collinear LSDA magnetic calculation (searched for possible stable magnetic configurations, in case the system was magnetic). For coherence, in the last step, all volumes were optimized using the LDA functional). Finally, the potential and density were expanded in plane-waves with a cutoff of $|\mathbf{G}| = 24/a_0$, and we set $R_{\min} \times |\mathbf{G} + \mathbf{k}|$ to 9, where R_{\min} is the smallest muffin-tin radius. The maximum angular momentum l for the expansion of the wave-function inside the muffin-tins set to 12. k -point grids were chosen with a minimum allowed spacing between k points of 0.15 in units of \AA^{-1} , equivalently to $14 \times 14 \times 8$ or more.

Atoms	Site	x	y	z	B (\AA^2)
Ba	4e	0	0	0.3556(1)	0.60(2)
Rh	2a	0	0	0	0.24(3)
O1	4c	0	0.5	0	1.0(1)
O2	4e	0	0	0.1522(7)	1.0(1)

Table I. Structural parameters for Ba_2RhO_4 . Space group $I4/mmm$ (No.139). $a = b = 4.0063(2)$ \AA , $c = 13.2966(8)$ \AA , $V = 213.42(2)$ \AA^3 . Reliability factors: $R_{wp} = 2.486$, $S = 1.95$.

III. RESULTS

A. Formation enthalpy of the 2-1-4 phase of Ba-Rh-O

Fig. 1 shows the convex hull of enthalpy formation calculated for stoichiometries between BaO–RhO₂, which can be found in the ternary phase diagram of Ba-Rh-O (see Fig. S1 in SM). At ambient pressure, the formation energy suggests that compositions such as Ba_2RhO_4 (2-1-4) and BaRhO_3 (1-1-3) are likely to be accessible to synthesis. Under pressures above 5 GPa, the 2-1-4 phase lowers its enthalpy, and is favorable with respect to the 1-1-3 phase (BaRhO_3), suggesting that could be stabilised upon the application of pressure. Our calculations also show that the Ruddlesden-Popper phases ($\text{Ba}_{n+1}\text{Rh}_n\text{O}_{3n+1}$) with bilayer ($n = 2$) and trilayer ($n = 3$) structures are not stable even at high pressures up to 20 GPa. Completing the Ruddlesden-Popper phase with $n = \infty$, the enthalpy reaches the highest value and matches the 1-1-3 in its cubic-perovskite phase. It is worth mentioning that in our results, the lowest enthalpy structure for the 1-1-3 phase is disputed between the hexagonal 6H and 4H structure motif below 20 GPa, and that only at very high pressures, the cubic perovskite phase dominates. Motivated by these findings, a high-pressure synthesis was carried out to find the stable 2-1-4 stoichiometry of the Ba-rhodate family (Sec. II A). We only attempted the synthesis of the 2-1-4 compositions, and after optimizing the synthesis conditions, structural and electrical measurements were carried out.

B. Structural properties

Fig. 2(c) shows the powder x-ray diffraction pattern of Ba_2RhO_4 , which was indexed on the basis of the tetragonal K_2NiF_4 -type structure with space group $I4/mmm$ [$a = 4.0063(2)$ \AA , $c = 13.2966(8)$ \AA]. The model of the Rietveld analysis is summarized in Table I, and the crystal structure is shown in Fig. 2(a). Another possible structural model with space group $I4_1/acd$, which allows rotation of the RhO_6 octahedra as in the case of Sr_2RhO_4 , can be ruled out by the absence of the visible reflections which are allowed and forbidden for the models with $I4/mmm$ and $I4_1/acd$, respectively (see Fig. S2 in

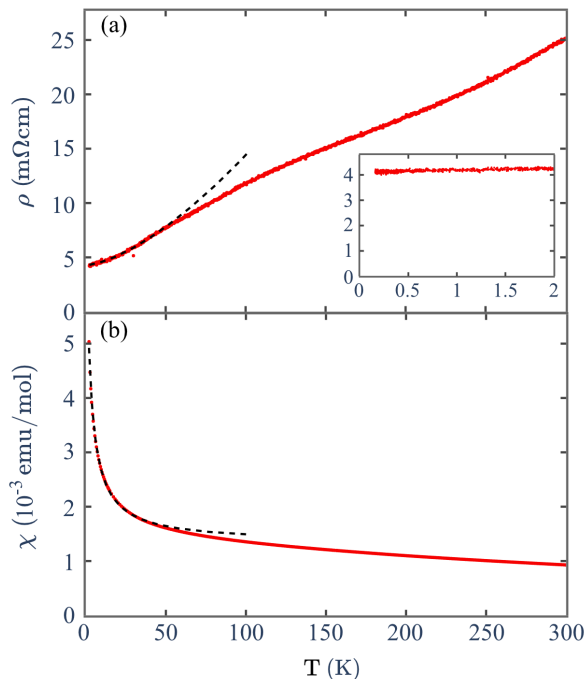


Figure 3. The temperature dependence of (a) electrical resistivity and (b) magnetic susceptibility for Ba_2RhO_4 , respectively. The green dashed line shows the fitting of the experimental data with $\rho = \rho_0 + AT^\alpha$, and $\chi = \chi_0 + C/(T + \theta)$ below 50 K, respectively. The inset of (a) shows no superconducting signals down to 0.16 K.

SM). Indeed, we confirmed that the reliability factors for $I4_1/acd$ are larger than for $I4/mmm$ (see Table SI). The Rh-O bond lengths 2.00–2.02 Å refined for $I4/mmm$ are fairly comparable to the value expected for that of $\text{Rh}^{4+}-\text{O}^{2-}$. On the other hand, as shown in Fig. 2(b), the refined Ba-O lengths are significantly shorter than the value 2.87 Å expected for the bond length between Ba^{2+} (1.47 Å for the nine-fold coordination) and O^{2-} ions (1.40 Å for the six-fold coordination)²⁴ indicating the compressed (over bonding) nature of the Ba-O bond. This feature points towards the metastable nature of the crystalline phase of Ba_2RhO_4 at ambient pressure.

C. Electrical resistivity, magnetic susceptibility, and specific heat capacity

The electrical resistivity and magnetic susceptibility as a function of temperature for Ba_2RhO_4 are shown in Fig. 3. Below 50 K, the electrical resistivity deviates from the T^2 dependence, expected for a Fermi liquid, and resistivity evolves as $\rho = \rho_0 + AT^\alpha$ with $\rho_0 = 4.25$ m Ωcm , $A = 9.24$ $\mu\Omega\text{cm}/\text{K}^2$, and $\alpha = 1.52$, which is in contrast to Sr_2RhO_4 with α comparable to or even larger than 2. Despite the apparent anomaly in α implying a non-Fermi liquid state, we cannot put in evidence its origin due to the polycrystalline nature of the material. It is also evi-

dent that we cannot conduct studies to rule out the possibility of anisotropy in the electrical resistivity inherent to the layered structure. In fact, the residual resistivity ρ_0 is relatively large as reported for the polycrystalline sample of Sr_2RhO_4 ,²⁵ presumably reflecting the grain boundary scattering and the layered structure. Interestingly, even decreasing the temperature down to 160 mK, no superconducting transition was observed [see the inset of Fig. 3(a)]. As shown in Fig. 3(b), a Curie-like tail is distinguishable below 50 K, and fitting the magnetic susceptibility with the expression $\chi = \chi_0 + C/(T + \theta)$ gives $\chi_0 = 1.33 \times 10^{-3}$ emu/mol, $C = 1.63 \times 10^{-2}$ emu/mol K, and $\theta = -2.55$ K. The C value is close to zero and no signal of magnetic transition is visible, indicating that a localized magnetic moment is absent in Ba_2RhO_4 .

The specific heat capacity of our Ba_2RhO_4 samples is shown in Fig. 4, and is compared to the reported ones of Sr_2RuO_4 and Sr_2RhO_4 ^{14,25}. The expected dominance of the linear electronic term is seen for both Ba_2RhO_4 and Sr_2RuO_4 below approximately 7 K. Between 2.0 and 7.5 K, the specific heat follows the equation $C/T = \gamma + (12/5)\pi^4 NR\Theta_D^3 T^2$ ($R = 8.31\text{J/molK}$ and $N = 1$), where γ and Θ_D represent an electronic specific heat coefficient and Debye temperature, respectively. Using this relation, we obtained the values of $\gamma = 36.56$ mJ/mol K^2 and $\Theta_D = 360$ K. The Debye temperature is comparable to that obtained by our first principle calculations (~ 320 K) and that of Sr_2RuO_4 (~ 410 K)²⁶. To be noted here is that the electronic specific heat is as large as that of Sr_2RuO_4 (~ 39 mJ/mol)³, implying that the electron correlation enhances the effective mass of conduction electrons. Here, we estimated the Wilson ratio R_w using the following expression,

$$R_w = \frac{\pi^2 k_B^2 \chi_0}{3\mu_B^2 \gamma}.$$

The estimated $R_w (= 2.64)$ is comparable to or even larger than the reported ones for Sr_2RuO_4 (~ 1.9) and Sr_2RhO_4 (~ 2.3), which are regarded as clean correlated electron metals^{14,27}. One should notice that the specific heat follows the above equation only in the narrow temperature range. Although the origin of the deviation at low temperature is elusive, the deviations below 4 K and above 7 K may suggest an electronic instability that violates the current Debye model.

D. Band structure and Fermi surface

Knowing that the 2-1-4 composition of Ba-Rh-O crystallizes in a layered-type structure similar to the 5d counterpart Ba_2IrO_4 , and the 4d, Sr_2RuO_4 , it is interesting to compare the electronic band structure near the valence energy among these materials. The Kohn-Sham band structure of Ba_2RhO_4 calculated within the local density approximation (LSDA) and including SOC (LSDA+SO) is shown in Fig. 5. To have a meaningful comparisons, we used their theoretical LDA-volume

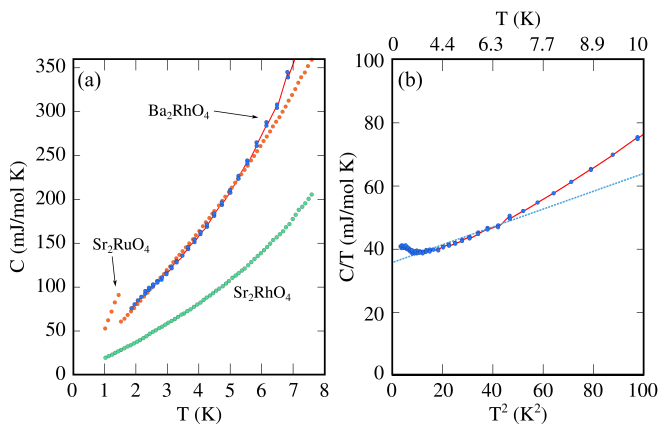


Figure 4. (a): Temperature dependence of the specific heat for Ba_2RhO_4 (blue dots), the reported of Sr_2RuO_4 (red dots) and Sr_2RhO_4 (green dots). (b): T^2 dependence of specific heat divided by temperature for Ba_2RhO_4 (blue dots). The blue dashed line shows the fitting of the experimental data with $T/C = \gamma + \beta T^2$ between 2.0 and 7.5 K.

and assumed a K_2NiF_4 -type structure for all cases. The band structure calculation, at the level of theory employed here, evidences a metallic and nonmagnetic character for Ba_2RhO_4 (see Table SII in SM), which is in agreement with our resistivity and magnetic measurements (see the calculated density of states presented in Fig. S3 in SM.). The case of Sr_2RuO_4 , a prototypical system in manifolds, has been vastly characterised and our calculations agree with the reported band structure for this system^{28–31}. Ba_2IrO_4 is an interesting case on which has been reported basal-plane antiferromagnetism^{12,32–35} at low temperatures and a Mott insulator transition is driven by the SOC³⁶. While the level of theory to treat this system is beyond the current employed in this work, in a simplified picture, we wanted to compare with the energy bands on the $5d$ -counter part. The orbital character and electronic symmetry of the bands are depicted as follows; the t_{2g} -dominated bands (d_{xy} , d_{xz} and d_{yz}) are in yellow and green shade, and the e_g ($d_{x^2-y^2}$) bands are shown in blur-blue.

As shown in Fig. 5, the electronic structure of Ba_2RhO_4 is closely related to the one of Sr_2RuO_4 , which has attracted a lot of attention for its possibility to emerge as a spin-triplet superconductor. However, the latest evidences suggest to disregard the chiral p -wave nature of the superconducting state of SrRuO_4 ^{5,37–39}. On the other hand, our new material, Ba_2RhO_4 has appealing differences evident around the Γ -point, where the e_g electron pocket descends the Fermi level, which is also found in Ba_2IrO_4 (using DFT-LSDA theory). A simple interpretation arises by looking at the position of the Fermi level in those systems; i.e., the electron counting of d bands in Ba_2RhO_4 is expected to be one more than that in Sr_2RuO_4 . Looking at the t_{2g} -dominated bands among the three compounds, and comparing to the NO-SOC bands (not shown) we can conclude that SOC plays

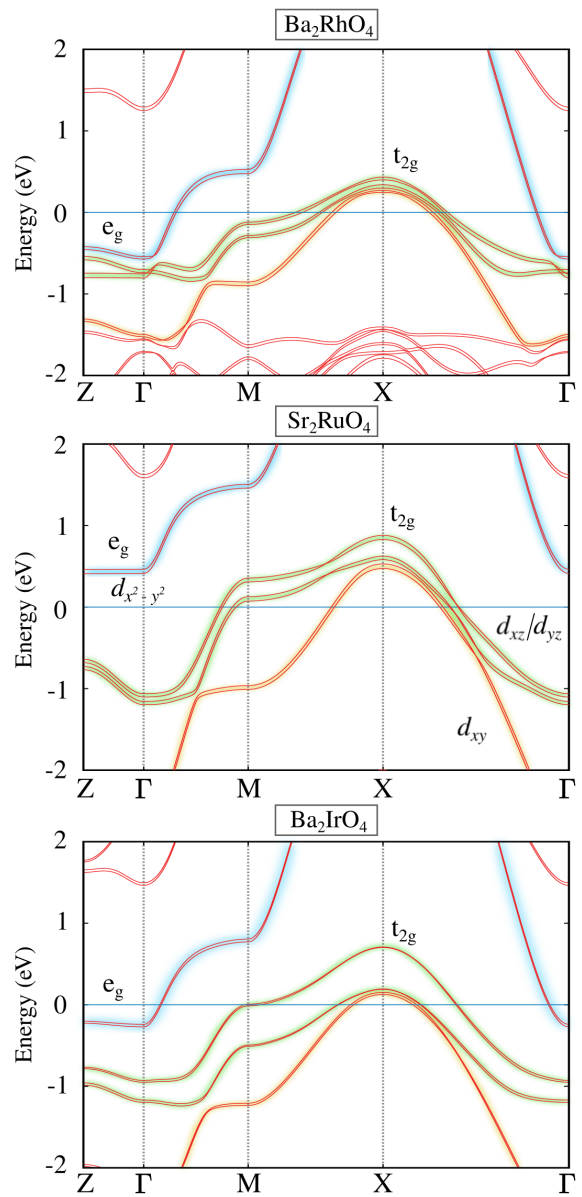


Figure 5. Full-potential DFT-LSDA band structure including spin-orbit coupling along selected high-symmetry points at zero pressure.

an important role on describing the splitting of d_{xz}/d_{yz} bands for the three compounds, while more marked differences arise for Sr_2RuO_4 and Ba_2IrO_4 . In Ba_2IrO_4 , the Mott insulator transition is driven by strong SOC, an effect that raises the bands opening a small band gap through a moderate Coulomb interaction. Although Ba_2RhO_4 is isoelectronic and isostructural with Ba_2IrO_4 , such a gap opening is hampered by the reduced SOC. Thus, $\text{Ba}_2\text{Rh}_{1-x}\text{Ir}_x\text{O}_4$ with the tetragonal structure can be an ideal system to investigate the SOC-induced metal-insulator transition¹⁷. As mentioned above, Ba_2RhO_4 is of peculiar interest, as it not only possesses inherent bands from the Ru-counterpart, but also shares the similar elec-

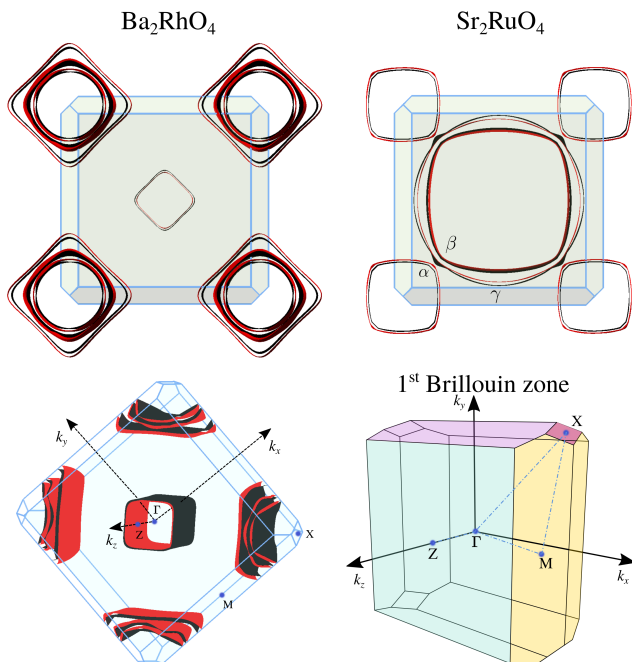


Figure 6. DFT-LSDA Fermi surfaces including spin-orbit coupling for Ba_2RhO_4 and Sr_2RuO_4 . two-dimensional projections are along k_z vector. The first Brillouin zone and selected high-symmetry points for the structure with $I4/mmm$ are shown.

tron bands from the $5d$ -Ir. These feature places Barhodate as strategic material that links the physics of $5d$ -oxides with $4d$ with a metallic character⁴⁰.

Understanding the topology of the Fermi surface of Ba_2RhO_4 is important to unravel the nature of electrons in the normal phase and possibly to shed light on the superconducting mechanism. Top panels in Fig. 6 show two-dimensional Fermi surfaces of Ba_2RhO_4 and Sr_2RuO_4 ^{41,42}. Left bottom panel includes a three-dimensional cut, and in the right, the first-Brillouin zone for the $I4/mmm$ -crystal as reference. The Fermi surface of Sr_2RuO_4 has been intensively investigated, both experimentally and theoretically²⁸⁻³¹. *Ab initio* calculations based on the local-density approximation qualitatively reproduce the Fermi surface topology, provided that the SOC is taken into account. Our calculation reproduces the well-studied Fermi surface of Sr_2RuO_4 , and also confirm that striking differences in the Fermi surface of Ba_2RhO_4 emerged. These difference are ascribed to the d -electron counting, and the electron pocket with e_g symmetry that pins below the Fermi level (see Fig. 5). It should be noted that the square-like tubular sheets along with X- Γ line can be regarded as quasi one-dimensional Fermi surface potentially yielding a nesting instability. More recently, LDA+DMFT (local-density approximation + dynamical mean-field theory) calculations have emphasized the interplay of Coulomb interaction and t_{2g} crystal field and the role of the Hund's rule coupling⁴³⁻⁴⁵. Besides, laser-based angle-resolved photo-

emission spectroscopy revealed the importance of SOC in Sr_2RuO_4 , and the self-energies estimation⁴⁶ for the β and γ -sheets were found to display significant angular dependence³⁰. In this study, we did not perform calculations with higher theory beyond standard DFT, hence we cannot rule out that similar effects are present in Ba_2RhO_4 . Finally, we also performed electron-phonon calculations for Ba_2RhO_4 using perturbation theory. The calculated phonon dispersion is shown in Fig. S4 in SM. The normal-state Eliashberg spectral function was adopted to estimate λ (the dimensionless strength of the electron-phonon coupling) and the phonon average ω_{log} . These calculations reveal a weak BCS superconductor, indeed our estimation of T_c is well-below 0.1 K, in agreement with the absence of any hint of superconductivity down to 0.16 K in our experiments. To find the superconducting phase of Ba_2RhO_4 , one might consider the possibility to further tune the electronic bands by applying pressure or by doing doping substitution, as recently reported for $\text{Sr}_{2-x}\text{La}_x\text{RhO}_4$ with a metal-insulator transition driven by a Lifshitz-transition¹⁸. To have an insight into the pressure dependence of the bands, we also verified the dependence of the electronic structure under isotropic compression, from 1 GPa to 20 GPa. Ba_2RhO_4 remains metallic well above 20 GPa, and the bands do not show any drastic change. The necessary pressure required to do a sizable change in the electronic structure is beyond 50 GPa. However, phase decomposition and other enthalpically phases might become more favourable. Another option to tune the bands with anisotropic pressure, i.e. due to the dimensionality of the layered perovskite phase, strain engineering via growth thins films is very attractive to search for the superconducting phase, proven that the synthetic route other than the current high pressure exists.

IV. CONCLUSIONS

Using a high pressure technique, a new layered perovskite-type oxide Ba_2RhO_4 was synthesized and quenched to ambient conditions, which was supported by the convex hull calculations. The crystal and electronic structure were characterized by both experimental and theoretical works. Ba_2RhO_4 indeed shares many of the Sr_2RuO_4 with interesting properties; layered structure, specific heat, magnetic properties and overall electronic features. The magnetic and resistivity measurements indicate that the system can be characterized as a correlated metal. Interestingly, the material does not show signs of superconductivity down to 0.16 K, which is supported by the theoretical estimation of the electron-phonon coupling. While the Fermi surface topology has reminiscent pieces of its Sr_2RuO_4 counterpart, one of the contrasting features in Ba_2RhO_4 is the presence of an electron e_g ($d_{x^2-y^2}$) band placed below the Fermi level, reflecting the increase in the d -electron counting. This feature provides a clue to discuss the role of electron cor-

relation on the stabilization of SOC-driven Mott insulating state in the isoelectronic and isostructural counterpart Ba_2IrO_4 . The new layered 2-1-4 perovskite phase, here reported for the first time⁴⁷, adds new possibilities to characterize $4d$ -electron physics, and bridges to the $5d$ -electron that is driven by SOC effects to Mott insulators⁴⁸. The anomalous increase in the specific heat capacity below 4K and the absence of superconductivity will be subject of future work, conceding single crystals can be synthesized.

V. ACKNOWLEDGMENTS

Computational resources were provided by the Swiss National Supercomputing Center withing the project s970. This study was supported in part by KAKENHI (Grant No. 17H01195, 17H06137, 19H02424, 16H06345, 19H05825, and 19K14652), the Asahi Glass Foundation, and Multidisciplinary Research Laboratory System for Future Developments in Osaka University. The synchrotron XRD measurement was performed with the approval of the Photon Factory Program Advisory Committee (Proposal No.2018S2-006). We acknowledge the Center for Computational Materials Science, Institute for Materials Research, Tohoku University for the use of MASAMUNE-IMR (MATERIALS science Supercomputing system for Advanced MULTi-scale simulations towards NExt-generation - Institute for Materials Research), Project No. 20S0023.

-
- ¹ R. J. Cava, van Dover RB, B. Batlogg, and E. A. Rietman, *Phys. Rev. Lett.* **58**, 408 (1987).
- ² J. B. Torrance, Y. Tokura, A. I. Nazzari, A. Beziinge, T. C. Huang, and S. S. P. Parkin, *Phys. Rev. Lett.* **61**, 1127 (1988).
- ³ Y. Maeno, H. Hashimoto, K. Yoshida, S. Nishizaki, T. Fujita, J. Bednorz, and F. Lichtenberg, *Nature* **372**, 532 (1994).
- ⁴ A. P. Mackenzie, T. Scaffidi, C. W. Hicks, and Y. Maeno, *npj Quantum Mater.* **2**, 532 (2017).
- ⁵ A. Pustogow, Y. Luo, A. Chronister, Y.-S. Su, D. A. Sokolov, F. Jerzembeck, A. P. Mackenzie, C. W. Hicks, N. Kikugawa, S. Raghu, E. D. Bauer, and S. E. Brown, *Nature* **574**, 72 (2019).
- ⁶ J. Matsuno, Y. Okimoto, Z. Fang, X. Z. Yu, Y. Matsui, N. Nagaosa, M. Kawasaki, and Y. Tokura, *Phys. Rev. Lett.* **93**, 167202 (2004).
- ⁷ M. K. Crawford, M. A. Subramanian, R. L. Harlow, J. A. Fernandez-Baca, Z. R. Wang, and D. C. Johnston, *Phys. Rev. B* **49**, 9198 (1994).
- ⁸ B. J. Kim, H. Jin, S. J. Moon, J.-Y. Kim, B.-G. Park, C. S. Leem, J. Yu, T. W. Noh, C. Kim, S.-J. Oh, J.-H. Park, V. Durairaj, G. Cao, and E. Rotenberg, *Phys. Rev. Lett.* **101**, 076402 (2008).
- ⁹ C. D. Dashwood, H. Miao, J. G. Vale, D. Ishikawa, D. A. Prishchenko, V. V. Mazurenko, V. G. Mazurenko, R. S. Perry, G. Cao, A. de la Torre, F. Baumberger, A. Q. R. Baron, D. F. McMorrow, and M. P. M. Dean, *Phys. Rev. B* **100**, 085131 (2019).
- ¹⁰ B. J. Kim, H. Ohsumi, T. Komesu, S. Sakai, T. Morita, H. Takagi, and T. Arima, *Science* **323**, 1329 (2009).
- ¹¹ H. Fukazawa, S. Nakatsuji, and Y. Maeno, *Physica B Condens. Matter* **281-282**, 613 (2000).
- ¹² H. Okabe, M. Isobe, E. Takayama-Muromachi, A. Koda, S. Takeshita, M. Hiraishi, M. Miyazaki, R. Kadono, Y. Miyake, and J. Akimitsu, *Phys. Rev. B* **83**, 155118 (2011).
- ¹³ M. Itoh, T. Shimura, Y. Inaguma, and Y. Morii, *J. Solid State Chem.* **118**, 206 (1995).
- ¹⁴ R. Perry, F. Baumberger, L. Balicas, N. Kikugawa, N. Ingle, A. Rost, J. Mercure, Y. Maeno, Z. Shen, and A. Mackenzie, *New J. Phys.* **8**, 175 (2006).
- ¹⁵ L. J. Sandilands, W. Kyung, S. Y. Kim, J. Son, J. Kwon, T. D. Kang, Y. Yoshida, S. J. Moon, C. Kim, and T. W. Noh, *Phys. Rev. Lett.* **119**, 267402 (2017).
- ¹⁶ M. W. Haverkort, I. S. Elfimov, L. H. Tjeng, G. A. Sawatzky, and A. Damascelli, *Phys. Rev. Lett.* **101**, 026406 (2008).
- ¹⁷ T. F. Qi, O. B. Korneta, L. Li, K. Butrouna, V. S. Cao, X. Wan, P. Schlottmann, R. K. Kaul, and G. Cao, *Phys. Rev. B* **86**, 125105 (2012).
- ¹⁸ J. Kwon, M. Kim, D. Song, Y. Yoshida, J. Denlinger, W. Kyung, and C. Kim, *Phys. Rev. Lett.* **123**, 106401 (2019).
- ¹⁹ F. Izumi and K. Momma (Trans Tech Publications Ltd, 2007) pp. 15–20.
- ²⁰ J. P. Perdew, K. Burke, and M. Ernzerhof, *Phys. Rev. Lett.* **77**, 3865 (1996).
- ²¹ G. Kresse and J. Furthmüller, *Comput. Mat. Sci.* **6**, 15 (1996).
- ²² K. Dewhurst *et al.*, “The Elk FP-LAPW Code,” (2015).
- ²³ K. Lejaeghere, G. Bihlmayer, T. Björkman, P. Blaha, S. Blügel, V. Blum, D. Caliste, I. E. Castelli, S. J. Clark, A. Dal Corso, *et al.*, *Science* **351** (2016).
- ²⁴ R. Shannon and C. Prewitt, *J. Inorg. Nucl. Chem.* **32**, 1427 (1970).
- ²⁵ K. Yamaura, Q. Huang, D. P. Young, and E. Takayama-Muromachi, *Chem. Mater.* **16**, 3424 (2004).
- ²⁶ S. Kittaka, S. Nakamura, T. Sakakibara, N. Kikugawa, T. Terashima, S. Uji, D. A. Sokolov, A. P. Mackenzie, K. Irie, Y. Tsutsumi, K. Suzuki, and K. Machida, *J. Phys. Soc. Jpn.* **87**, 093703 (2018).
- ²⁷ A. Georges, L. d. Medici, and J. Mravlje, *Annu. Rev. Condens. Matter Phys.* **4**, 137 (2013).
- ²⁸ T. Oguchi, *Phys. Rev. B* **51**, 1385 (1995).
- ²⁹ Z. Wang, D. Walkup, P. Derry, T. Scaffidi, M. Rak, S. Vig, A. Kogar, I. Zeljkovic, A. Husain, L. H. Santos, Y. Wang, A. Damascelli, Y. Maeno, P. Abbamonte, E. Fradkin, and V. Madhavan, *Nat. Phys.* **13**, 799 (2017).

- ³⁰ A. Tamai, M. Zingl, E. Rozbicki, E. Cappelli, S. Riccò, A. de la Torre, S. McKeown Walker, F. Y. Bruno, P. D. C. King, W. Meevasana, M. Shi, M. Radović, N. C. Plumb, A. S. Gibbs, A. P. Mackenzie, C. Berthod, H. U. R. Strand, M. Kim, A. Georges, and F. Baumberger, *Phys. Rev. X* **9**, 021048 (2019).
- ³¹ N.-O. Linden, M. Zingl, C. Hubig, O. Parcollet, and U. Schollwöck, *Phys. Rev. B* **101**, 041101(R) (2020).
- ³² Y. Hou, H. Xiang, and X. Gong, *New J. Phys.* **18**, 043007 (2016).
- ³³ C. Martins, M. Aichhorn, and S. Biermann, *J. Phys. Condens. Matter* **29**, 263001 (2017).
- ³⁴ R. Arita, J. Kuneš, A. V. Kozhevnikov, A. G. Eguiluz, and M. Imada, *Phys. Rev. Lett.* **108**, 086403 (2012).
- ³⁵ C. Martins, M. Aichhorn, L. Vaugier, and S. Biermann, *Phys. Rev. Lett.* **107**, 266404 (2011).
- ³⁶ S. Moser, L. Moreschini, A. Ebrahimi, B. Dalla Piazza, M. Isobe, H. Okabe, J. Akimitsu, V. V. Mazurenko, K. S. Kim, A. Bostwick, E. Rotenberg, J. Chang, H. M. Rønnow, and M. Grioni, *New J. Phys.* **16**, 013008 (2014).
- ³⁷ K. Ishida, M. Manago, K. Kinjo, and Y. Maeno, *J. Phys. Soc. Japan* **89**, 034712 (2020).
- ³⁸ S. Benhabib, C. Lupien, I. Paul, L. Berges, M. Dion, M. Nardone, A. Zitouni, Z. Q. Mao, Y. Maeno, A. Georges, L. Taillefer, and C. Proust, *Nat. Phys.* (2020), 10.1038/s41567-020-1033-3.
- ³⁹ S. Ghosh, A. Shekhter, F. Jerzembeck, N. Kikugawa, D. A. Sokolov, M. Brando, A. P. Mackenzie, C. W. Hicks, and B. J. Ramshaw, *Nat. Phys.* (2020), 10.1038/s41567-020-1032-4.
- ⁴⁰ W. Witczak-Krempa, G. Chen, Y. B. Kim, and L. Balents, *Annu. Rev. Condens. Matter Phys.* **5**, 57 (2014).
- ⁴¹ J. Wu, H. P. Nair, A. T. Bollinger, X. He, I. Robinson, N. J. Schreiber, K. M. Shen, D. G. Schlom, and I. Božović, *Proc. Natl. Acad. Sci.* **117**, 10654 (2020).
- ⁴² W. Huang and H. Yao, *Phys. Rev. Lett.* **121**, 157002 (2018).
- ⁴³ M. Malvestuto, E. Carleschi, R. Fittipaldi, E. Gorelov, E. Pavarini, M. Cuoco, Y. Maeno, F. Parmigiani, and A. Vecchione, *Phys. Rev. B* **83**, 165121 (2011).
- ⁴⁴ G. Zhang, E. Gorelov, E. Sarvestani, and E. Pavarini, *Phys. Rev. Lett.* **116**, 106402 (2016).
- ⁴⁵ O. Gingras, R. Nourafkan, A.-M. S. Tremblay, and M. Côté, *Phys. Rev. Lett.* **123**, 217005 (2019).
- ⁴⁶ J. J. Deisz and T. E. Kidd, *Phys. Rev. B* **95**, 045122 (2017).
- ⁴⁷ C. K. Poole, H. A. Farach, and R. J. Creswick, *Handbook of superconductivity* (Elsevier, 1999).
- ⁴⁸ D. Pesin and L. Balents, *Nat. Phys.* **6**, 376 (2010).